

# Precision Spectroscopy of Deeply Bound Pionic Atoms and Partial Restoration of Chiral Symmetry in Medium

Natsumi IKENO<sup>1</sup>, Rie KIMURA<sup>1</sup>, Junko YAMAGATA-SEKIHARA<sup>2,3</sup>, Hideko NAGAIHIRO<sup>1</sup>, Daisuke JIDO<sup>3</sup>, Kenta ITAHASHI<sup>4</sup>, Li Sheng GENG<sup>5,6</sup> and Satoru HIRENZAKI<sup>1</sup>

<sup>1</sup>*Department of Physics, Nara Woman's University, Nara 630-8506, Japan*

<sup>2</sup>*Departamento de Física Teórica and IFIC, Centro Mixto Universidad de Valencia-CSIC, Institutos de Investigación de Paterna, Aptdo. 22085, 46071 Valencia, Spain*

<sup>3</sup>*Yukawa Institute for Theoretical Physics, Kyoto University, Kyoto 606-8502, Japan*

<sup>4</sup>*Nishina Center for Accelerator-Based Science, RIKEN, 2-1 Hirosawa, Wako, 351-0198 Saitama, Japan*

<sup>5</sup>*School of Physics and Nuclear Energy Engineering, Beihang University, Beijing 100191, China*

<sup>6</sup>*Physik Department, Technische Universität München, D-85747 Garching, Germany*

We study theoretically the formation spectra of deeply bound pionic atoms expected to be observed by experiments with high energy resolution at RIBF/RIKEN, and we discuss in detail the possibilities to extract new information on the pion properties at finite density from the observed spectra, which may provide information on partial restoration of chiral symmetry in medium. We find that the non-yrast pionic states such as  $2s$  are expected to be seen in the  $(d, {}^3\text{He})$  spectra, which will be helpful to reduce uncertainties of the theoretical calculations in the neutron wave functions in nucleus. The observation of the  $2s$  state with the ground  $1s$  state is also helpful to reduce the experimental uncertainties associated in the calibration of the absolute excitation energy. We find that the nuclear densities probed by atomic pions are quite stable and almost constant for various atomic states and various nuclei. Effects of the pion wave function renormalization to the formation spectra are also evaluated.

## §1. Introduction

Properties of hadrons at finite density and temperature are extremely interesting in the contemporary hadron-nuclear physics because they provide important hints to explore the relation between the symmetry breaking pattern of QCD and the observed hadron properties for the study of the QCD vacuum structure.<sup>1)</sup> One of the good systems to observe in-medium hadron properties is the deeply bound pionic atom,<sup>2),3)</sup> which is a  $\pi^-$  atomic bound state hardly observed by X-ray spectroscopy, such as the  $1s$  or  $2p$  states in heavy nuclei. The deeply bound states have been experimentally produced in the  $(d, {}^3\text{He})$  reactions with Pb and Sn isotope targets at GSI<sup>4)-7)</sup> by following theoretical predictions.<sup>8)-12)</sup> In the latest experiment,<sup>7)</sup> the energy shifts and widths of the  $1s$  states have been precisely measured in three Sn isotopes and isospin-density dependence of the  $s$ -wave pion-nucleus potential has

been deduced. From these observations, reduction of the chiral order parameter  $\langle \bar{q}q \rangle$  in nucleus was concluded. A recent model independent theoretical analysis supported the way to extract the in-medium quark condensate from the pionic atom data and showed a relation connecting the in-medium quark condensate to the hadronic observables.<sup>13)</sup> For further studies of in-medium pion properties, new experiments were proposed to make high precision spectroscopy of pionic atoms systematically in RIBF/RIKEN.<sup>14),15)</sup> Thus, the pionic atom can be one of the best systems to deduce the quantitative results for the meson properties and the partial restoration of chiral symmetry in medium around normal nuclear density at zero temperature.

Based on these theoretical and experimental developments, we think that we should consider now the possible future directions of the studies of the deeply bound pionic atoms after 15 years from the discovery of the deeply bound pionic atoms at GSI.<sup>4),5),16),17)</sup> We discuss the following points in this article in detail,

- (i) Predictions of the pionic atom formation spectra by the  $(d, {}^3\text{He})$  reactions on Sn and Te isotope targets proposed in Refs. 14), 15) at RIBF/RIKEN,
- (ii) Possibility to observe pion properties and to determine the value of the chiral condensate at different nuclear density from  $\rho = 0.6\rho_0$  to obtain information on the symmetry breaking parameters beyond the linear density approximation,
- (iii) Possibility to determine the wave function renormalization factor introduced in Refs. 13) and 18) from pionic atom observables,
- (iv) Uncertainties included in theoretical calculations used to evaluate formation cross sections,

with paying the attention to the advantages of the simultaneous observation of the non-yrast  $2s$  bound state together with the deepest  $1s$  state for the same nucleus in the new experiments with better energy resolution.<sup>14),15)</sup>

In Section 2, we summarize the theoretical formalism used to connect the pion properties to the order parameter of the chiral symmetry and the wave function renormalization factor. We also mention the sensitivities of atomic pion to nuclear densities and the strong correlation between potential parameters. In Section 3, we show the numerical results and discussions for the structure and formation of deeply bound pionic atoms. Section 4 is devoted to the conclusion. We summarize the supplementary formalisms and numerical results in Appendixes.

## §2. Formalism

We introduce briefly the formula reported in Ref. 13) in this section as the guide to deduce the information on chiral symmetry from the pionic atoms observables. We also mention the sensitivities of atomic pions to nuclear density and the strong correlation of the potential parameters. The theoretical formula used in this article to calculate the structure and the formation cross sections of the pionic atoms are summarized in Appendix A.

### 2.1. Chiral Dynamics of Pionic Atoms

The spontaneously broken chiral symmetry in vacuum is expected to be restored partially in nuclear medium. The partial restoration of chiral symmetry takes place

with effective reduction of the chiral quark condensate  $\langle \bar{q}q \rangle$  in medium.<sup>19),20)</sup> Experimental observation of the reduction of the quark condensate is not so trivial, since the quark condensate is not a direct observable. In Ref. 7) K. Suzuki *et al.* made use of in-medium extensions of the two well-known relations, Gell-Mann-Oakes-Renner (GOR) relation<sup>21)</sup> and Tomozawa-Weinberg relation (TW),<sup>22),23)</sup> to connect the quark condensate and the observables in pionic atoms, after having extracted the values of the parameters in the optical potential from the observed energy shifts and widths of the deeply bound atomic states. The  $b_1$  parameter of the optical potential in Eq. (A.5) corresponds to the effective scattering length between pion and nucleus, which can be expressed by an in-medium extended TW relation:

$$T_{\pi A}^{(-)} = -4\pi\epsilon_1 b_1 = \frac{\omega}{2f_\pi^{*2}}, \quad (2.1)$$

where  $f_\pi^*$  is an in-medium pion decay constant. Assuming that the pion mass does not change in nucleus, one could have an in-medium GOR relation

$$m_\pi^2 f_\pi^{*2} = -2m_q \langle \bar{q}q \rangle_\rho, \quad (2.2)$$

where  $m_q$  is the isospin-averaged quark mass  $m_q = (m_u + m_d)/2$  and  $\langle \bar{q}q \rangle_\rho$  is the in-medium quark condensate. Using these two relations, K. Suzuki *et al.*<sup>7)</sup> could get a connection between the experimental observation and the in-medium quark condensate through  $b_1$  and  $f_\pi^*$ .

The experimental observations of the deeply bound pionic states and the attempt to connect the observables to  $\langle \bar{q}q \rangle_\rho$  based on the simple extension of the in-vacuum relations have stimulated theoretical works to give stronger foundations of the analysis. It was shown based on chiral perturbation theory<sup>18)</sup> and on a correlation function analysis<sup>13)</sup> that the in-medium TW relation Eq. (2.1) can be valid in the linear approximation of the isovector density, which leads to

$$\frac{b_1^{\text{free}}}{b_1} = \left( \frac{f_\pi^t}{f_\pi} \right)^2, \quad (2.3)$$

with the in-vacuum isovector  $\pi N$  scattering length  $b_1^{\text{free}}$ , the in-vacuum pion decay constant  $f_\pi$  and the time component of the in-medium pion decay constant  $f_\pi^t$ . Further, it was found in a model-independent argument based on the operator relation that there is a sum rule for the in-medium quark condensate.<sup>13)</sup> This sum rule can be simplified at low density limit and gives a new scaling relation

$$\frac{\langle \bar{q}q \rangle_\rho}{\langle \bar{q}q \rangle} = Z_\pi^{*1/2} \left( \frac{f_\pi^t}{f_\pi} \right), \quad (2.4)$$

where  $Z_\pi^*$  is the wave function renormalization for the in-medium pion (see also Ref. 24)). The density dependence of the wave function renormalization can be estimated at low density limit through the  $\pi N$  scattering amplitude<sup>13)</sup>:

$$Z_\pi^* = 1 - \beta\rho, \quad (2.5)$$

with  $\beta = 2.17 \pm 0.04 \text{ fm}^3$ . Combining Eqs. (2.3) and (2.4), one obtains a connection between the in-medium quark condensate and the experimental observables as

$$\frac{\langle \bar{q}q \rangle_\rho}{\langle \bar{q}q \rangle} = Z_\pi^{*1/2} \left( \frac{b_1^{\text{free}}}{b_1} \right)^{1/2}. \quad (2.6)$$

The  $b_1$  parameter in Eq. (2.6) is obtained by the pionic atom data, and the rest in the right hand side,  $b_1^{\text{free}}$  and  $Z_\pi^*$ , are evaluated by the  $\pi N$  scattering. For completeness, it is very good if one can determine also the wave function renormalization from the deeply bound pionic atoms instead of using the in-vacuum  $\pi N$  scattering. We discuss the possibility to determine the pion wave function renormalization factor from the observation of the pionic atom states in Section 3.3. We also mention here that the estimation of the higher order effects of the density from experimental data is also interesting and important to explore the behavior of  $\langle \bar{q}q \rangle_\rho$  beyond the linear density approximation.<sup>25)-27)</sup> The discussion of the possibility to deduce the higher order effects from the observation will be given in Section 3.2.

## 2.2. Nuclear densities probed by atomic pion and Seki-Masutani correlations

As we will see in detail in Section 3.2, the pion in atomic states observed by the X-ray spectroscopy are known to be only sensitive to narrow range of nuclear density, which is almost independent of the nuclides and the atomic states.<sup>28)</sup> Hence, the structure of the pionic atoms is essentially determined by the optical potential strength at the effective nuclear density  $\rho_e$  probed by atomic pion. Namely, the series of optical potentials which have the same potential strength at  $\rho = \rho_e$  equivalently provide the almost same structure of the pionic atoms. As a consequence, we have a certain relation between potential parameters of the optical potentials which reproduce the atomic data well. We consider the  $s$ -wave part of the optical potential  $V_s$  as an example which includes the important piece  $b_1$  to deduce the  $\langle \bar{q}q \rangle_\rho$  value and plays the dominant role for the deeply bound  $s$  states.<sup>12)</sup> The  $s$ -wave optical potential for the symmetric nuclei  $\rho_n = \rho_p$  is written as,

$$2\mu V_s(r) = -4\pi[\varepsilon_1 b_0 \rho(r) + \varepsilon_2 B_0 \rho^2(r)]. \quad (2.7)$$

For all  $b_0$  and  $B_0$  values satisfying the relation

$$b_0 + \frac{\varepsilon_2}{\varepsilon_1} \rho_e B_0 = \text{constant}, \quad (2.8)$$

the optical potential (2.7) has the same strength at  $\rho = \rho_e$  and provide almost same structure of the pionic atoms. Actually the correlations between potential parameters are found phenomenologically and called as the Seki-Masutani (SM) correlations.<sup>29)</sup>

The SM correlations are expressed as;

$$b_0 + \alpha_s B_0 = \beta_s = (-0.03 + 0.01i) \text{m}_\pi^{-1}, \quad \alpha_s \simeq 0.23 \text{m}_\pi^3, \quad (2.9)$$

and

$$\frac{c_0 + \alpha_p C_0}{\gamma} = \beta_p = (-0.2 + 0.02i) \text{m}_\pi^{-3}, \quad \alpha_p \simeq 0.37 \text{m}_\pi^3, \quad (2.10)$$

where,

$$\gamma = 1 + \frac{4}{3}\pi\lambda c_0\rho_e. \quad (2.11)$$

The parameters  $b_0, B_0, c_0$ , and  $C_0$  determine the strength of the pion-nucleus optical potential shown in Eq. (A.4). Seki and Masutani found that the series of potential parameter sets, which satisfy the relations (2.9) and (2.10), reproduce the observed data by the X-ray spectroscopy reasonably well. Namely, it is very difficult to fix the unique set of potential parameters from the data taken by the X-ray experiments. In the modern  $\chi^2$  analyses of the data, one can expect the unique determination of the potential parameters and, actually, one may find literatures which report the unique determination. However, there still remain the strong SM correlations, and the  $\chi^2$ -values in these analyses have the long deep valley structure along the SM relations of potential parameters.

We can find from Eqs. (2.8) and (2.9) as,

$$\rho_e = \frac{\varepsilon_1}{\varepsilon_2}\alpha_s, \quad (2.12)$$

and the value of  $\alpha_s$  determined by the analyses of atomic data indicates,

$$\rho_e \simeq \frac{1}{2}\rho_0. \quad (2.13)$$

Hence, it means that the SM correlation found phenomenologically is the consequence of the fact that the nuclear density probed by various pionic atoms observed by X-ray is always close to  $\frac{1}{2}\rho_0$ . This feature is also found for some of the deeply bound pionic states,<sup>3),28)</sup> and thought to be one of the robust features of pionic states. In the early stage of the exploration of deeply bound pionic atoms, this robustness was an advantage to deduce the pion properties at  $\rho_e \simeq \frac{1}{2}\rho_0$ , however, to make a step further, we need to investigate the possibility to deduce the pion properties precisely not only at  $\rho_e \simeq \frac{1}{2}\rho_0$  but also at various nuclear densities. If we can determine  $\langle\bar{q}q\rangle_\rho$  for various densities, it is expected to provide important experimental information for the studies of the chiral condensate beyond the linear density approximation.

### §3. Numerical Results and Discussions

In this section, we investigate how we can deduce the  $\langle\bar{q}q\rangle$  value at finite density precisely from pionic atom data. As already mentioned,  $\langle\bar{q}q\rangle$  was determined in Ref. 7), however, the recent theoretical work provide a different formula including the  $Z_\pi^*$  factor as introduced in Section 2.1. In addition, the  $\langle\bar{q}q\rangle$  value was determined only at  $\rho \sim 0.6\rho_0$  because of the limited sensitivity of the observed pionic atom data to nuclear density, which is related to Seki-Masutani correlations to the potential parameters as mention in Section 2.2. Thus, we study theoretically these points to find the proper way to deduce the  $\langle\bar{q}q\rangle$  value for various densities from the future observations. We also pay attention to the possible simultaneous observation of the non-yrast  $2s$  state with the deepest  $1s$  state.<sup>14),15)</sup>

### 3.1. ( $d, {}^3\text{He}$ ) spectra in experiments

We first show the comparison of the theoretical calculations with the latest data of the pionic atom formation in Sn isotopes. In Fig. 1, we show the calculated results together with experimental data reported in Ref. 7). The instrumental resolution is assumed to be  $\Delta E = 394$  keV FWHM (Full Width Half Maximum) as same as the data.<sup>7)</sup> We added the constant background to the calculated results and then scaled the calculated spectra to reproduce the strength of the resonance peak of the  $1s$  state formation in the experimental data for this resolution. We also show the calculated results using the same theoretical model with the improved resolution  $\Delta E = 150$  keV FWHM which is expected to be archived in the planned experiments.<sup>14), 15)</sup> We find that the theoretical calculation reproduce the experimental data reasonably well and provide the reliable interpretation of the spectra, which is an essential foundation of the research activity to deduce the pion properties from the ( $d, {}^3\text{He}$ ) spectra. And as we can see from the figure, we conclude that the pionic  $2s$  state can be observed as a peak structure together with the  $1s$  state in the experiments with the better resolution  $\Delta E = 150$  keV FWHM. This result helps to propose the new experimental activity and motivate us to proceed the theoretical analyses reported in this article.

Simultaneous observation of the non-yrast  $2s$  state with the ground  $1s$  state is of essential importance in the experimental viewpoints. We expect smaller experimental uncertainty in the energy difference between the two states while larger ambiguities are usually associated in the calibration of the absolute excitation energy.

In order to resolve the two states  $1s$  and  $2s$  in the excitation spectrum, the spectral energy resolution  $\Delta E$  must be improved by a factor of about two from  $\sim 400$  keV to  $\sim 200$  keV. The resolution is governed by two major contributions, namely the incident beam energy spread and the energy loss in the target. The latter can be controlled by changing the target thickness. However, adaptation of thinner target results in smaller statistical merits or in longer data accumulation periods unless the beam intensity is increased as compensation.

A new experimental approach is thus started<sup>15)</sup> in the RI beam factory, RIKEN<sup>30)</sup> to achieve improved resolution of 200 keV with much higher statistics. The experiment makes full use of the very high intensity deuteron beam of  $\sim 1 \times 10^{12}$ /second, which is more than 30 times higher than the previously available intensity in the SIS-18 accelerator in the GSI. Thus, the statistical merit is still huge even if the adopted target thickness of  $5 \text{ mg/cm}^2$  is factor of three smaller than the previous experiments, and the larger luminosity is essential for systematic study over wide range of nuclei. The other contribution in the energy resolution, the incident beam energy spread, is  $\sim 5$  times larger in the RIBF. Elaborate study on the accelerator, the beam transfer line, and the spectrometer is ongoing to establish a dispersion matching beam optics where the contribution of the beam energy spread is suppressed in the excitation spectra.<sup>31)</sup>

Simultaneous observation of the  $2s$  state with the  $1s$  state is important also in the theoretical viewpoints. As shown in detail in Appendix B, the uncertainties of the theoretical calculation of the pionic atom formation cross sections due to the neutron wave function and the nuclear excited levels could be an obstacle to

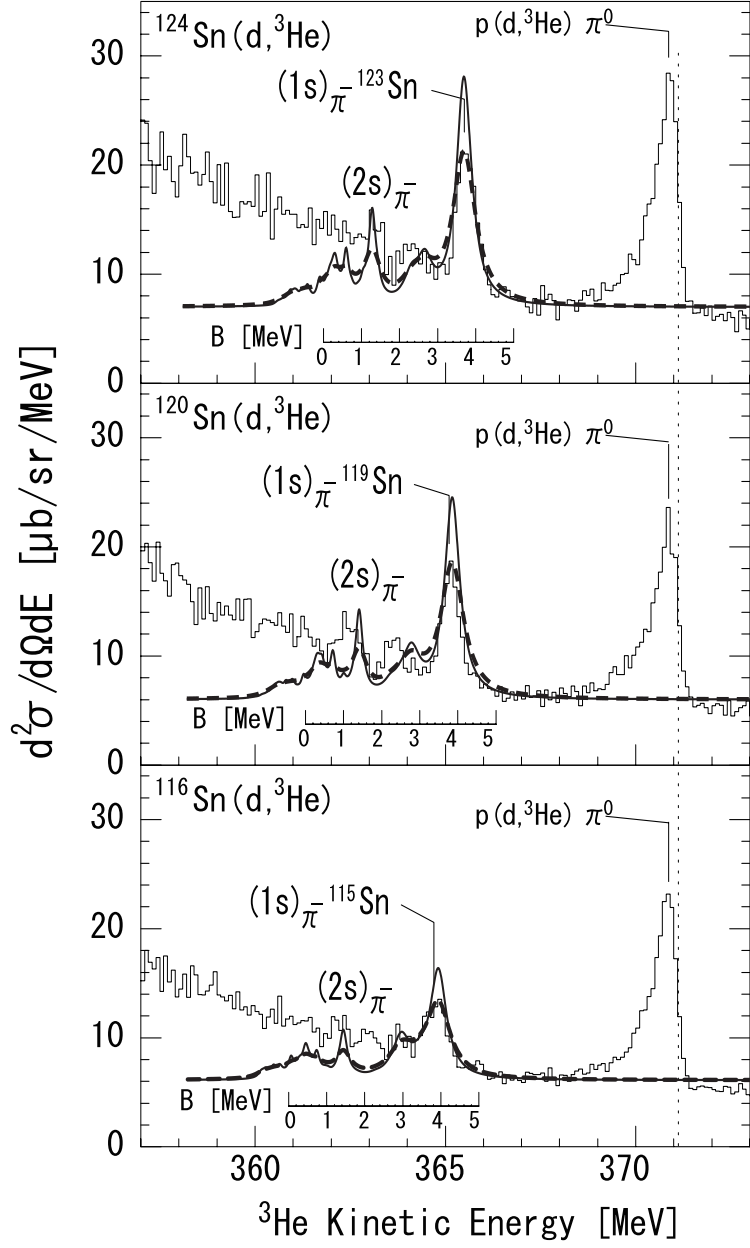


Fig. 1. The  $(d,^3\text{He})$  spectra for the formation of the deeply bound pionic states in Sn isotopes as indicated in figure. The solid and dashed lines denote the theoretical calculations, which include only bound state contributions, while the histogram shows observed experimental data.<sup>7)</sup> The instrumental energy resolution is assumed to be  $\Delta E = 394$  keV FWHM for the dashed lines and 150 keV FWHM for the solid lines. The calculated results are scaled to reproduce the strength of the  $1s$  state formation peak in the observed spectra for  $\Delta E = 394$  keV FWHM.

deduce the properties of pion by the precision measurements. Thus, as a practical way to reduce the uncertainties and deduce the reliable results, we should make use

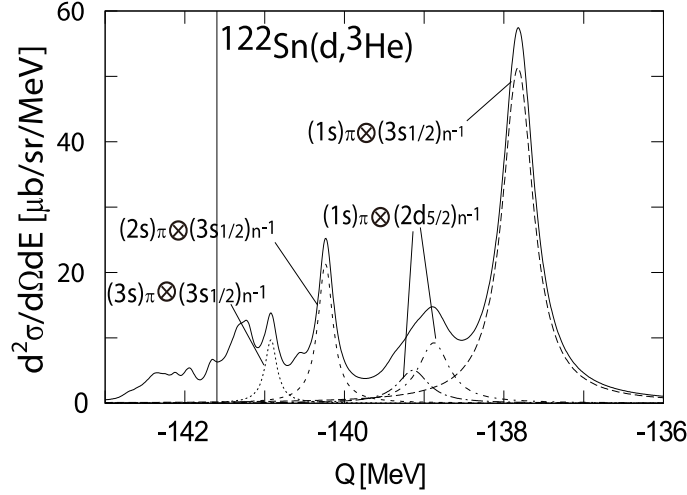


Fig. 2. Calculated  $^{122}\text{Sn}(d, ^3\text{He})$  spectra for the formation of the pionic bound states at  $T_d = 500\text{MeV}$  are shown as functions of the reaction  $Q$ -value, where the  $F_O$  factors in Table V are used. The dominant subcomponents are also shown as indicated in the Figure. Instrumental energy resolution is assumed to be 150 keV FWHM. The vertical line indicates the threshold  $Q = -141.6\text{ MeV}$ .

of the recoilless kinematics to populate the plural number of pionic states coupled with the same neutron hole state as dominant contributions in the  $(d, ^3\text{He})$  spectra. And by comparing the strength of these contributions, we can effectively remove the ambiguities due to the structure of the target nucleus, the nuclear excited levels, and the neutron wave functions. In this context, the simultaneous observation of  $1s$  and  $2s$  pionic states coupled with the  $(3s_{1/2})_n^{-1}$  neutron hole is very interesting. We show the calculated  $^{122}\text{Sn}(d, ^3\text{He})$  spectra in Fig. 2. This reaction is proposed in Refs. 14), 15). As we can see from the figure, the  $1s$  and  $2s$  pionic states coupled with the same  $(3s_{1/2})_n^{-1}$  neutron hole state can be seen as the clear peak structures with the realistic energy resolution  $\Delta E = 150\text{ keV}$  FWHM. Thus, the  $^{122}\text{Sn}(d, ^3\text{He})$  reaction can be one of the good reactions for our purpose. The expected spectra for Te isotopes are summarized in Appendix D.

### 3.2. Determination of $b_1$ parameter at various nuclear density

As shown in Ref. 7), the observed binding energies and widths of bound pions have been used to determine the strength of the  $s$ -wave isovector potential parameter ( $b_1$ ). The important points we should address here are to find out the way to determine  $b_1$  value at various densities to know its density dependence beyond the linear form.

First, we consider the effective nuclear density probed by atomic pion.<sup>28)</sup> The effective nuclear density  $\rho_e$  is defined as the nuclear density at the radial coordinate  $r_e$  as  $\rho_e = \rho(r_e)$ , where the overlapping density,

$$S(r) = \rho(r) |R_{nl}(r)|^2 r^2, \quad (3.1)$$

has the maximum value. Here,  $R_{nl}(r)$  is the radial wave function of the pionic atom



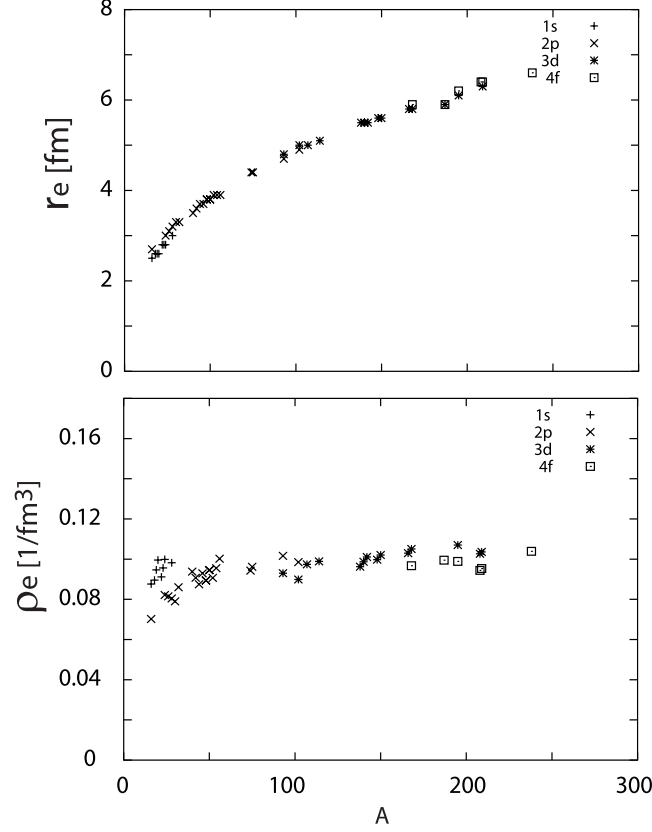


Fig. 3. Calculated peak positions  $r_e$  (upper frame) and the corresponding effective nuclear densities  $\rho_e$  (lower frame) for the observed pionic atom states by X-ray experiments are plotted as functions of nuclear mass number  $A$ . The quantum numbers of each atomic state are indicated in the figure.

in a state of  $(nl)$ . The definition of the overlapping density  $S(r)$  indicates that it is expected to evaluate the sensitivity of the iso-scalar  $s$ -wave optical potential term to the energy eigen values in the sense of the first order perturbation theory. In Fig. 3, we show the calculated  $r_e$  and  $\rho_e$  systematically for the pionic atom states which have been observed by the experiments of the X-ray spectroscopy, so far.<sup>32)</sup> As shown in the figure,  $r_e$  increased with the nuclear mass number  $A$  monotonically, however  $\rho_e$  is almost constant (‘saturated’) except for the very light nuclear cases. These features, which are almost independent on the quantum numbers of the states, can be understood by the pocket structure of the potential for the atomic pion and the localization of the overlapping densities there as can be seen in Appendix C. Thus, all pionic atoms observed by the X-ray experiments probed the almost same nuclear density nearly independent on the nuclide and the quantum numbers of the pion except for the pionic states in the light nuclei. Thus, it seems that all observations of these states only provide pion properties around  $0.6\rho_0$ . To obtain pion properties at various nuclear densities, it will be necessary to observe other states.

Then, we consider the atomic states in  $^{121}\text{Sn}$  up to  $n = 6$  including the deeply

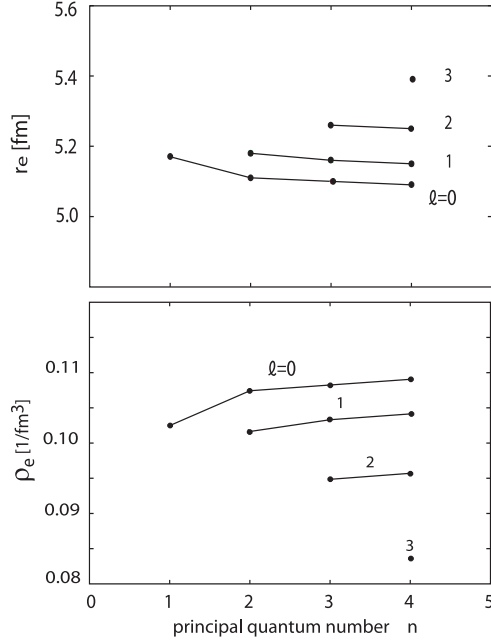


Fig. 4. Peak positions  $r_e$  (upper frame) of the overlapping densities  $S(r)$  and the corresponding effective nuclear densities  $\rho_e$  (lower frame) of  $^{121}\text{Sn}$ .

bound and non-yrast states, which can not be observed in X-ray experiments. When we use the Coulomb wave functions for bound pions,  $\rho_e$  distributed in relatively wide range  $0.05 \lesssim \rho_e \lesssim 0.16 \text{ [fm}^{-3}]$  depending on the bound states. As naturally expected, the states with smaller orbital angular momentum  $\ell$  tend to probe the larger nuclear densities. As the realistic cases, we show the results calculated with the optical potential in Fig. 4.  $\rho_e$  and  $r_e$  only change inside the smaller range than those calculated with Coulomb potential only. This behavior can be also understood by the picture of the potential pocket and the localization of the overlapping densities at the nuclear surface. Thus, we find that the effective nuclear density is rather stable ( $0.08 \lesssim \rho_e \lesssim 0.11 \text{ [fm}^{-3}]$ ) even for the non-yrast states and the deeply bound states.

We mention here that an interesting tendency appeared in Fig. 4 that the states with higher  $n$  for a fixed  $\ell$  provide larger  $\rho_e$  values contrast to the usual intuitions. This is because of the larger tunneling effects to the central soft core for more lightly bound states. Thus, the sensitivity of pion in the higher  $n$  states moves to higher  $\rho$ , however at the same time, the absolute magnitude of the strong interaction effects are reduced rapidly as  $n$  increases. For example, we may think that it is better to observe the  $4s$  and  $4f$  states to probe pion properties in different nuclear densities from Fig. 4. This will be wrong since the strong interaction effects are too small for both states and the  $p$ -wave interaction plays dominant role in  $f$  states<sup>12)</sup> and hides the  $b_1$  effects even they may provide information for different  $\rho$ .

Hence, we find that the observation of the binding energies of the pionic atoms will provide the pion properties near  $\rho \sim 0.6\rho_0$ . Thus, to deduce the density dependence of the  $b_1$  parameter, we require the extremely higher energy resolution data

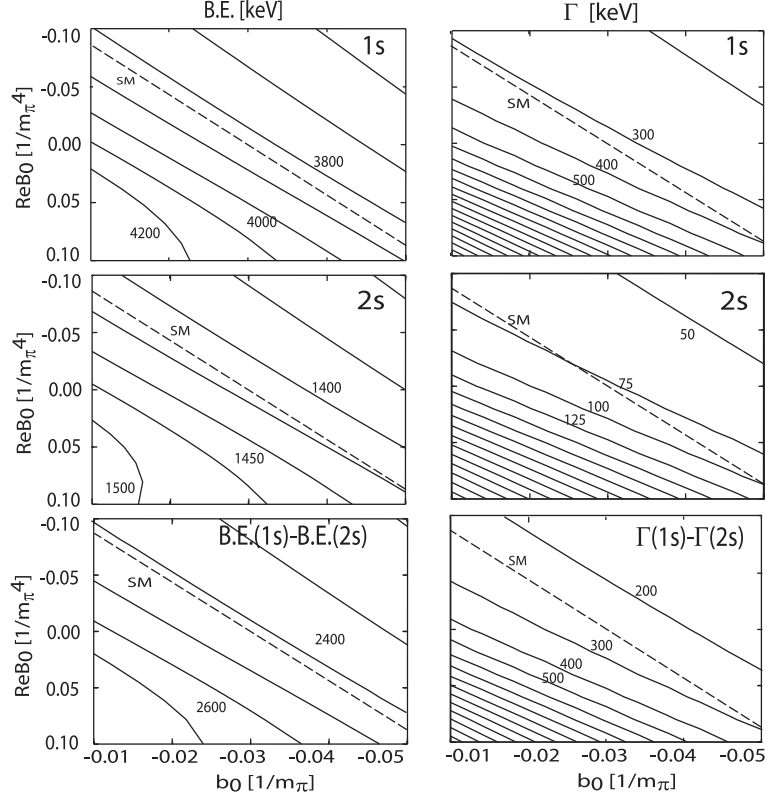


Fig. 5. Contour plots of the binding energies (left) and widths (right) for the 1s (upper) and 2s (middle) states, and the difference of 1s and 2s states (lower) in  $^{121}\text{Sn}$  in the  $b_0$ - $\text{Re}(B_0)$  plane. The dashed lines depicted by SM are the parameter sets satisfying the Seki and Masutani correlation.<sup>29)</sup> The numbers in the figure indicate the values of the binding energy and width of contour lines in unit of keV.

as we will see later in the discussion with energy contour plots in this section.

We, then, consider the contour plots of the binding energies B.E. and widths  $\Gamma$  of 1s and 2s pionic states in  $\pi^- - ^{121}\text{Sn}$  system. By the contour plots of eigen energies, we can see the difference of the sensitivities to the nuclear density as the deviations from the SM correlation and we can see the required energy resolution to distinguish the pion properties at different  $\rho$ . The contour plots of the differences of the binding energy and width of 1s and 2s states are also shown, which could be used to deduce the systematic errors due to the calibration of the absolute binding energies and the uncertainties of the neutron distribution of  $^{121}\text{Sn}$ . We mention here that the binding energies and widths of the 1s states in Sn isotopes were precisely determined in the last experiment.<sup>7)</sup> For example, the binding energy and width of the 1s state in  $^{123}\text{Sn}$  are  $\text{B.E.} = 3.744 \pm 0.018$  [MeV] and  $\Gamma = 0.341 \pm 0.072$  [MeV].<sup>7)</sup>

We show the numerical results in Fig. 5 in  $b_0$ - $\text{Re}B_0$  plane together with the SM correlation line Eq. (2.9). We find that the contour lines for the binding energy of 1s state are almost parallel to the SM line. Since the slope of the contour lines in  $b_0$ - $\text{Re}B_0$  plane provide the information of the nuclear density probed by the atomic

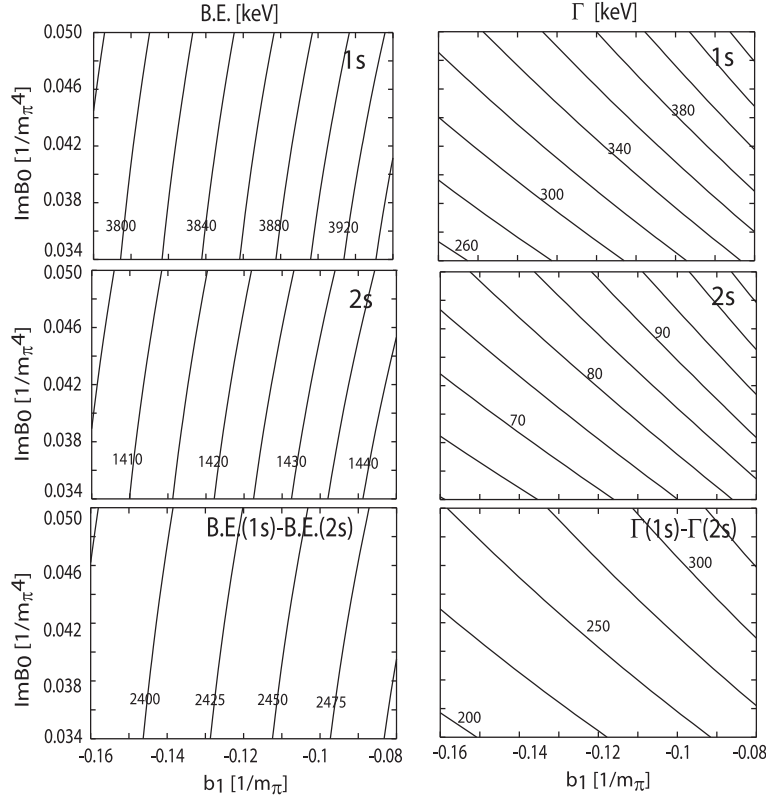


Fig. 6. Contour plots of the binding energies (left) and widths (right) for the 1s (upper) and 2s (middle) states, and the difference of 1s and 2s states (lower) in  $^{121}\text{Sn}$  in the  $b_1$ - $\text{Im}(B_0)$  plane. The numbers in the figure indicate the values of the binding energy and width of contour lines in unit of keV.

pion as shown in Eqs. (2.9) and (2.12), this feature indicates that the nuclear density mainly probed by the 1s state is very close to  $\alpha_s$  as shown in Eq. (2.12), and that the precise measurements of the 1s state provide the medium effects of pion at  $\alpha_s$ . In addition, it is very hard to determine the unique parameter set ( $b_0, \text{Re}B_0$ ) on the SM line only from the observation of 1s state.

On the other hand, the contour lines of the 2s state show the slightly different slope from that of the SM line. This behavior indicates that the properties of the 2s state are determined by the pion properties at slightly different nuclear density from  $\alpha_s$  as indicated by the result shown in Fig 4. And we may be able to find the unique parameter set ( $b_0, \text{Re}B_0$ ) by using the both B.E. of 1s and 2s states with high precision. The plots of the difference of the binding energies of 1s and 2s states, which is expected be observed with high precision without systematic errors due to the absolute energy calibration, show the similar behavior of that of the 1s state because the larger binding energy value of the 1s states dominate the behavior of the plot. We may also expect that the uncertainties due to the neutron distribution are partly cancelled in the plots of the energy differences.

In principle, to determine the  $b_1$  value for different  $\rho$  by observing the atomic states, we need to distinguish the nuclear density observed by these states, which will be equivalent to fixing the unique set of  $\{b_0, \text{Re}B_0\}$  by data, and then to determine  $b_1$  value independently for each state. Thus, the experimental data with very high precision are necessary to obtain  $b_1$  values at various  $\rho$  as indicated in Fig. 5.

The contour plots of the widths show different behavior from those of the binding energies, and the contour lines are not parallel to the SM line for all three cases shown in the right panels in Fig. 5. To understand this behavior intuitively is a little difficult since this is the effect to the imaginary eigenvalues from the modifications of the real part of the potential. However, we can naively expect that the  $\rho^2$  behavior of the imaginary potential can provide the different sensitivity of the widths of the pionic states from that of the binding energies. The contour plots of widths indicate that the precise determinations of the pionic widths will provide the constraints to the potential parameters, though the determinations of the widths are more difficult in general than those of the binding energies.

In Fig. 6, we show another contour plot in  $b_1 - \text{Im}B_0$  plane. The  $b_1$  parameter is one of the most important parameters and has the very close relation to  $\langle \bar{q}q \rangle$ , and the  $\text{Im}B_0$  parameter is the leading term to determine the width  $\Gamma$  in the  $s$ -states. The contour of the binding energy indicates the reasonable independence of B.E. on  $\text{Im}B_0$ , while the contour of the width indicates the complexity of the behavior of the width which depends strongly both on  $\text{Im}B_0$  and  $b_1$ . The contour of the binding energy shows a clear relation between the accuracy of the binding energy data and the  $b_1$  parameter determination.

One possible way to deduce the  $b_1$  values for different  $\rho$  is the parameter search using the most precise experimental data of the atomic  $s$  states, which are most sensitive to the  $s$  wave potential parameters,<sup>12)</sup> allowing the different value of  $b_1$  for each states. Since this procedure, in principle, require to distinguish the nuclear densities observed by the atomic states to determine the different  $b_1$  values for these states independently, the precisions of the data should be so high that we can clearly determine the  $b_0$  and  $B_0$  parameter uniquely and, thus, the feasibility of this procedure highly depends on the precision of the pionic atom data.

### 3.3. ( $d, {}^3\text{He}$ ) spectra and observation of $Z_\pi^*$

The purpose of this section is to investigate the possibilities to determine the wave function renormalization factor  $Z_\pi^*$  shown in Section 2.1 from the observation of the formation cross section of the deeply bound pionic atoms. The basic idea is to observe the change of the cross section due to the modification of the pion wave function  $\phi_{l_\pi}$  as,

$$\phi_{l_\pi}(\mathbf{r}) \rightarrow \phi_{l_\pi}^R(\mathbf{r}) = Z_\pi^{*1/2} \phi_{l_\pi}(\mathbf{r}), \quad (3.2)$$

due to the renormalization factor  $Z_\pi^*$  originated from the energy dependence of the pion selfenergy. The modification of the wave function causes the change of the the cross section as shown in Appendix A.  $Z_\pi^*$  is associated with the pion selfenergy in nuclear medium and, hence, has the  $\rho(r)$  dependence as shown in Eq. (2.5) in contrast to that appeared in the standard text book of field theory. Due to the  $\rho(r)$  dependence of  $Z_\pi^*$ , we can expect to have different effects of  $Z_\pi^*$  for the formation

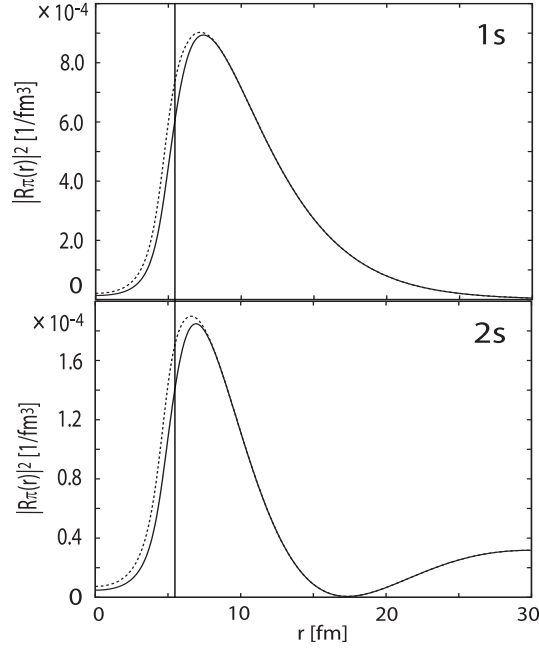


Fig. 7. Pion radial density distributions  $|R_\pi(r)|^2$  are shown as functions of the radial coordinate  $r$  for  $1s$  and  $2s$  states in  $^{121}\text{Sn}$ . Solid and dotted lines show the pion density evaluated by the radial part of the renormalized ( $\phi^R$ ) and unrenormalized ( $\phi$ ) wave functions defined in Eq. (3.2), respectively. The vertical line indicates the nuclear half radius  $R = 5.4761$  fm.

Table I. The calculated effective numbers of  $[(1s)_\pi \otimes (3s_{1/2})_n^{-1}]$  and  $[(2s)_\pi \otimes (3s_{1/2})_n^{-1}]$  subcomponents by renormalized and unrenormalized pion wave functions defined in Eq. (3.2) in PWIA. The ratios of the effective numbers of  $1s$  and  $2s$  pionic states are also shown.

pion wave function	$N_{\text{eff}}(1s)$	$N_{\text{eff}}(2s)$	$N_{\text{eff}}(1s)/N_{\text{eff}}(2s)$
$\phi_{l_\pi}^R(r)$	$1.36 \times 10^{-1}$	$2.92 \times 10^{-2}$	4.66
$\phi_{l_\pi}(r)$	$1.41 \times 10^{-1}$	$3.00 \times 10^{-2}$	4.70

Table II. Same as Table I except for the results in DWIA.

pion wave function	$N_{\text{eff}}(1s)$	$N_{\text{eff}}(2s)$	$N_{\text{eff}}(1s)/N_{\text{eff}}(2s)$
$\phi_{l_\pi}^R(r)$	$2.05 \times 10^{-2}$	$4.09 \times 10^{-3}$	5.01
$\phi_{l_\pi}(r)$	$2.08 \times 10^{-2}$	$4.17 \times 10^{-3}$	4.99

cross sections of different subcomponents  $[\ell_\pi \otimes j_n^{-1}]$  in general.

We show in Fig. 7 the pion radial densities of  $1s$  and  $2s$  states in  $^{121}\text{Sn}$  calculated by  $\phi^R$  and  $\phi$  in Eq. (3.2). Because  $Z_\pi^*$  is one outside the nucleus, the pion densities are modified only inside the nucleus  $0 \leq r \lesssim 8$  fm as can be seen in Fig 7. In Fig. 8, we show the contributions of  $(3s_{1/2})_n^{-1}$  neutron-hole state to the  $^{122}\text{Sn}(d, ^3\text{He})$  spectra for the formation of pionic atoms and we find the effects due to  $Z_\pi^*$  factor are tiny. To estimate the effects of  $Z_\pi^*$  to the observables, we show the calculated effective

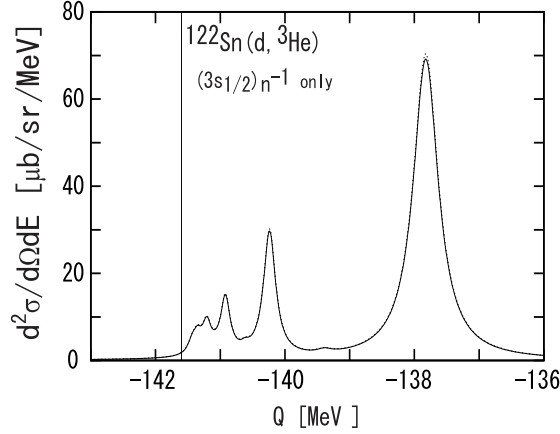


Fig. 8. Contributions of the  $(3s_{1/2})_n^{-1}$  neutron hole state to the  $^{122}\text{Sn}(d, {}^3\text{He})$  spectra for the formation of the pionic bound states are shown as functions of the reaction  $Q$ -value. The  $F_O$  and  $F_R$  factors are fixed to be 1. The solid line shows the calculated results with the renormalized pion wave function ( $\phi^R$ ) and the dotted line that with the unrenormalized wave function ( $\phi$ ) defined in Eq. (3.2). The vertical line indicates the threshold  $Q = -141.6$  MeV.

numbers for the dominant subcomponents  $[(1s)_\pi \otimes (3s_{1/2})_n^{-1}]$  and  $[(2s)_\pi \otimes (3s_{1/2})_n^{-1}]$  in Tables I and II. We find that the ratios  $N_{\text{eff}}(1s)/N_{\text{eff}}(2s)$  of  $N_{\text{eff}}$  of pion  $1s$  and  $2s$  states formation, which are expected to be good quantities to deduce the pion properties independent on the uncertainties of the neutron wave function as discussed in Appendix B, changes only around 1% for PWIA and 0.4 % for DWIA for results with  $\phi^R$  and  $\phi$ . These numbers seem to be too small to observe experimentally at present. Actually, the variation of the ratio of effective number  $N_{\text{eff}}(1s)/N_{\text{eff}}(2s)$  due to the uncertainties of neutron wave function is larger and is around 10% as discussed in Appendix B. Hence, it seems difficult to deduce new information on  $Z_\pi^*$  from the observed spectra by simply using the ratio of  $1s$  and  $2s$  states formation strength. We mention here that the effects of  $Z_\pi^*$  in the ratios of  $N_{\text{eff}}$  are suppressed because the pionic  $1s$  and  $2s$  states probe the almost same nuclear density as described in Section 3.2 and the  $Z_\pi^*$  effects for both states are cancelled out in the ratio. The idea to extract new information on  $Z_\pi^*$  from observables are considered to be still relevant.

Finally, we also investigate the sensitivity of the neutron pick-up reactions to the optical potential parameters which satisfy the Seki-Masutani correlation Eq. (2.9). Since the effective numbers calculated by Eq. (A.10) have different  $\phi_{l_\pi}$  dependence from the overlapping density Eq. (3.1), we may have chance to distinguish the potential parameters with Seki-Masutani correlation by the formation cross sections. We consider three sets of  $b_0$  and  $\text{Re}B_0$  parameter which are,  $\{b_0, \text{Re}B_0\} = \{-0.0185, -0.05\}$ ,  $\{-0.0300, 0.00\}$ , and  $\{-0.0415, 0.05\}$ , where parameters are in pion mass units, and we find that there appear some discrepancies in the radial part of the integrand of Eq. (A.10) around  $0 \leq r \lesssim 4.5$  fm. Since the nuclear half radius is taken to be 5.4761 fm in this case, the discrepancy only exists deep inside the nucleus which will be significantly suppressed by the distortion factor. Thus, we expect

that the effects to the formation rate are extremely small. We have confirmed the expectation by numerical calculation which show that the variation of the ratios of the effective numbers of  $1s$  and  $2s$  states for these potential parameter sets is less than 1 %.

#### §4. Conclusion

In this article, we have shown the newly calculated  $(d, {}^3\text{He})$  spectra on the  ${}^{122}\text{Sn}$ ,  ${}^{122}\text{Te}$ ,  ${}^{126}\text{Te}$  targets for the formation of the pionic atoms.<sup>14),15)</sup> Based on these results, we have investigated the possibilities to deduce the new information on the  $\langle \bar{q}q \rangle$  value at various nuclear densities and on the wave function renormalization factor  $Z_\pi^*$  paying attention to the recent theoretical and experimental developments of the studies of the pionic atoms.

We have found that the formation spectra on the  ${}^{122}\text{Sn}$  target is suited for the observation of the pionic states because of the simple neutron level structure and large occupation probability of  $3s_{1/2}$  neutron state. However, the  $(d, {}^3\text{He})$  reaction on Te isotopes could include the extra difficulties due to the complex neutron level structure and should be considered carefully for the experiments.

We have also found that the nuclear density probed by the atomic pion is distributed only inside the narrow region around  $\rho = 0.6\rho_0$  even for the deeply bound pionic states and the non-yrast states. This feature had an advantage in early stage of the exploration, however, it requires now the experimental data with excellent precision to deduce the information on  $\langle \bar{q}q \rangle$  at various nuclear density as shown in the contour plot studies in Section 3.2.

As for the uncertainties of the calculated cross sections and the determination of  $Z_\pi^*$ , we have found that the ratio of the subcomponents coupled with the same neutron hole state is a good index relatively free from the systematic errors due to the neutron wave function. This observation is possible in experiments in RIBF/RIKEN. However, the renormalization factor  $Z_\pi^*$  changes the pion wave function inside the nucleus slightly and the effects to the cross section are masked by the distortion factor. Since the nuclear densities probed by atomic pions are around  $0.6\rho_0$ , the effects of  $Z_\pi^*$  for various pionic atoms are almost same and are cancelled out in the ratio of the formation cross sections. Hence, the observation of  $Z_\pi^*$  is rather difficult at preset. However, the idea to deduce  $Z_\pi^*$  information from observables is important and the further studies are required.

We think that we need to consider the pionic atoms in exotic nuclei to obtain the pion properties at various nuclear densities and the information on pion wave function renormalization. For example, the existence of the pionic nuclear states due to the strong Coulomb attraction<sup>33)</sup> and due to the thick neutron skin effects<sup>34)</sup> were predicted theoretically. Pionic atoms in unstable nuclei were studied in various cases in Refs. 35)–37). In these systems with exotic nuclei, we may have the different sensitivities of pions to nuclear densities and the different effects of the renormalization factor to the formation spectra. We will leave the study of these systems as future works.



### Acknowledgements

We would like to thank H. Toki, T. Yamazaki, R. S. Hayano and K. Suzuki for many collaborations and fruitful discussions on the pionic atoms. N. I. appreciates the support by the Grant-in-Aid for JSPS Fellows. This work was partly supported by the Grants-in-Aid for Scientific Research (No. 22740161, No. 20540273, No. 22105510, and No. 22105517). This work was done in part under the Yukawa International Program for Quark-hadron Sciences (YIPQS).

### Appendix A

#### — Theoretical Formula for Structure and Formation of Pionic Atoms —

The theoretical formula to calculate the structure and formation of the pionic atoms<sup>2), 3), 8)–12)</sup> are summarized in this Appendix. The energy spectra and wave functions of the pionic atoms can be obtained theoretically by solving the Klein-Gordon equation,

$$[-\nabla^2 + \mu^2 + 2\mu V_{\text{opt}}(r)] \phi(\mathbf{r}) = [E - V_{\text{coul}}(r)]^2 \phi(\mathbf{r}), \quad (\text{A}\cdot 1)$$

where  $\mu$  is the pion-nucleus reduced mass,  $E$  the eigen energy written as  $E = \mu - B_\pi - \frac{i}{2}\Gamma$  with the binding energy  $B_\pi$  and the width  $\Gamma$  of the atomic states. The  $V_{\text{coul}}$  is the Coulomb potential with a finite nuclear charge density distribution  $\rho_{ch}(r)$ :

$$V_{\text{coul}}(r) = -e^2 \int \frac{\rho_{ch}(r')}{|\mathbf{r} - \mathbf{r}'|} d\mathbf{r}'. \quad (\text{A}\cdot 2)$$

The charge density distribution is written by the Woods-Saxon form as,

$$\rho_{ch}(r) = \frac{\rho_{ch0}}{1 + \exp[(r - R_{ch})/a_{ch}]}. \quad (\text{A}\cdot 3)$$

The parameters of the charge distributions are taken from Ref. 38) and summarized in Table III for the nuclei considered in this article.

The  $V_{\text{opt}}$  in Eq. (A.1) is the pion-nucleus optical potential, which we assume to be of the Ericson-Ericson type,<sup>39)</sup>

$$2\mu V_{\text{opt}}(r) = -4\pi[b(r) + \varepsilon_2 B_0 \rho^2(r)] + 4\pi \nabla \cdot [c(r) + \varepsilon_2^{-1} C_0 \rho^2(r)] L(r) \nabla, \quad (\text{A}\cdot 4)$$

with

$$b(r) = \varepsilon_1 [b_0 \rho(r) + b_1 [\rho_n(r) - \rho_p(r)]], \quad (\text{A}\cdot 5)$$

$$c(r) = \varepsilon_1^{-1} [c_0 \rho(r) + c_1 [\rho_n(r) - \rho_p(r)]], \quad (\text{A}\cdot 6)$$

$$L(r) = \left\{ 1 + \frac{4}{3} \pi \lambda [c(r) + \varepsilon_2^{-1} C_0 \rho^2(r)] \right\}^{-1}, \quad (\text{A}\cdot 7)$$

where  $\varepsilon_1$  and  $\varepsilon_2$  are defined as  $\varepsilon_1 = 1 + \frac{\mu}{M}$  and  $\varepsilon_2 = 1 + \frac{\mu}{2M}$  with the nucleon mass  $M$ . As a standard parameter set, we use the potential parameters listed in Table IV,

Table III. Radius parameters  $R_{ch}$  of the charge distributions taken from Ref 38). The diffuseness parameters are fixed to be  $a_{ch} = t/4\ln 3$  for all nuclei with  $t = 2.30$  fm.

nuclide	$^{116}\text{Sn}$	$^{120}\text{Sn}$	$^{122}\text{Sn}$	$^{124}\text{Sn}$	$^{122}\text{Te}$	$^{126}\text{Te}$
$R_{ch}$ [fm]	5.4173	5.4588	5.4761	5.4907	5.5368	5.5617

which are taken from Ref. 29). We use the Woods-Saxon form for the distributions of proton and neutron centers and assume the same shape for the both distributions,

$$\rho(r) = \rho_p(r) + \rho_n(r) = \frac{\rho_0}{1 + \exp[(r - R)/a]}, \quad (\text{A}\cdot 8)$$

where  $R$  and  $a$  are the radius and diffuseness parameters, which are determined from the parameters  $R_{ch}$  and  $a_{ch}$  of the charge distributions  $\rho_{ch}$  by the prescription described in Ref. 40). For the calculations of the bound states, we use the distribution parameters  $R$  and  $a$  same as the target nuclei of the  $(d, {}^3\text{He})$  formation reaction. The  $\rho_0$  is obtained by the correct normalization of the mass number of the daughter nucleus.

Table IV. Pion-nucleus optical potential parameters<sup>29)</sup> used in the present calculations.

$b_0 = -0.0283m_\pi^{-1}$	$b_1 = -0.12m_\pi^{-1}$
$c_0 = 0.223m_\pi^{-3}$	$c_1 = 0.25m_\pi^{-3}$
$B_0 = 0.042im_\pi^{-4}$	$C_0 = 0.10im_\pi^{-6}$
$\lambda = 1.0$	

We can calculate the pionic atom formation cross sections in the effective number approach<sup>8),9)</sup> using the pionic atom wave function  $\phi_{l\pi}$ , the binding energy  $B_\pi$ , and the width  $\Gamma$  obtained by solving the Klein-Gordon equation Eq. (A.1). The  $(d, {}^3\text{He})$  reaction cross section in the laboratory frame is expressed as,

$$\left(\frac{d\sigma}{d\Omega dE}\right)_{dA \rightarrow {}^3\text{He}(A-1)\pi} = \left(\frac{d\sigma}{d\Omega}\right)_{dn \rightarrow {}^3\text{He}\pi} \times \sum_{[l_\pi \otimes j_n^{-1}]} \frac{\Gamma}{2\pi} \frac{1}{\Delta E^2 + \Gamma^2/4} N_{\text{eff}}, \quad (\text{A}\cdot 9)$$

with

$$N_{\text{eff}} = \sum_{JMm_s} \left| \int d\mathbf{r} d\sigma \chi_f^*(\mathbf{r}) \xi_{1/2, m_s}^*(\sigma) [\phi_{l_\pi}^* \otimes \psi_{j_n}(\mathbf{r}, \sigma)]_{JM} \chi_i(\mathbf{r}) \right|^2. \quad (\text{A}\cdot 10)$$

Here,  $\left(\frac{d\sigma}{d\Omega}\right)_{dn \rightarrow {}^3\text{He}\pi}$  indicates the elementary differential cross section at forward angles for the  $d + n \rightarrow {}^3\text{He} + \pi^-$  reaction in the laboratory system, which is extracted from the experimental data of the  $p + d \rightarrow \pi^+ + t$  reaction assuming charge symmetry.<sup>8),9)</sup>  $\Delta E$  is defined as  $\Delta E = Q + m_\pi - B_\pi + S_n - 6.787$  MeV for the  $(d, {}^3\text{He})$  reaction with the pion mass  $m_\pi$ , the pion binding energy  $B_\pi$ , the neutron separation energy  $S_n$ , and the reaction  $Q$ -value.  $\Gamma$  denotes the width of the bound pionic state.

For the neutron wave function  $\psi_{j_n}$ , we adopt the harmonic-oscillator (HO) wave function in this article for simplicity. We also use the calculated neutron wave

function with Woods-Saxon type potential to check the theoretical uncertainties of the cross sections in Appendix B. We have used the oscillator parameter given by  $\hbar\omega = 40A^{-\frac{1}{3}}$  MeV for the harmonic-oscillator wave functions, with  $A$  the nuclear mass number. The spin wave function is denoted as  $\xi_{1/2,m_s}(\sigma)$ , and we take the spin average with respect to  $m_s$  so as to take into account the possible spin direction of the neutrons in the target nucleus.  $\chi_i$  and  $\chi_f$  express the initial and final distorted waves of the projectile and the ejectile, respectively. We use the Eikonal approximation and replace  $\chi_i$  and  $\chi_f$  according to

$$\chi_f^*(\mathbf{r})\chi_i(\mathbf{r}) = \exp(i\mathbf{q} \cdot \mathbf{r})D(z, \mathbf{b}), \quad (\text{A}\cdot 11)$$

where the distortion factor  $D(z, \mathbf{b})$  is defined as

$$D(z, \mathbf{b}) = \exp \left[ -\frac{1}{2}\sigma_{dN} \int_{-\infty}^z dz' \rho_A(z', \mathbf{b}) - \frac{1}{2}\sigma_{hN} \int_z^{\infty} dz' \rho_{A-1}(z', \mathbf{b}) \right]. \quad (\text{A}\cdot 12)$$

Here, the deuteron-nucleon and  $^3\text{He}$ -nucleon total cross sections are denoted as  $\sigma_{dN}$  and  $\sigma_{hN}$ . The function  $\rho_A(z, \mathbf{b})$  and  $\rho_{A-1}(z, \mathbf{b})$  are the density distributions of the target and daughter nuclei at beam-direction coordinate  $z$  with impact parameter  $\mathbf{b}$ . The effective number approach is sometimes called the distorted wave impulse approximation (DWIA), and also called the plane wave impulse approximation (PWIA) in case we neglect the distortion effects in Eqs. (A.11) and (A.12) as putting  $D(z, \mathbf{b}) = 1$ .

In order to predict the spectrum of the  $(d, ^3\text{He})$  reactions, we need to take into account the realistic ground-state configurations of the target nuclei, the excitation energies, and the relative excitation strengths leading to the excited states of the daughter nuclei. To obtain a realistic total strength for the neutron pick-up from each orbital, we need to normalize the calculated effective numbers using the neutron occupation probabilities in the ground state of the target nucleus. The occupation probabilities are obtained from the analyses of the  $^AZ(d, t)^{A-1}Z$  reaction data and are not equal to one in general.

As for the excited levels of the daughter nuclei, we use the experimental excitation energies and strengths obtained from the  $^AZ(d, t)^{A-1}Z$  reaction. Since the single-neutron pick-up reaction from a certain orbital in the target can couple to several excited states of the daughter nuclei, we need to distribute the effective numbers among these excited levels of the daughter nuclei in proportion to the experimental strengths. Thus, the effective number for the pionic state  $(\ell_\pi)$  formation with the  $N$ -th daughter nucleus excited state coupled to a single neutron pick-up from a neutron orbit  $j_n$  is written

$$N_{\text{eff}}(\ell_\pi \otimes (j_n^{-1})_N) = N_{\text{eff}}(\ell_\pi \otimes j_n^{-1}) \times F_O(j_n) \times F_R((j_n^{-1})_N), \quad (\text{A}\cdot 13)$$

where  $N_{\text{eff}}(\ell_\pi \otimes j_n^{-1})$  is the effective number defined in Eq. (A.10),  $F_O$  the normalization factor due to the occupation probabilities of the neutron states  $j_n$  in the target nucleus, and  $F_R$  is the relative strength of the  $N$ -th excited states in the daughter nucleus coupled to the single neutron pick-up from the state  $j_n$ . The  $F_O$  and  $F_R$  of some medium heavy nuclei are compiled in Tables V, VI, IX, and X given in Appendixes B and D, and also in Refs. 11), 12).

## Appendix B

### — Nuclear Structure Dependence of Formation Cross Section of Pionic Atoms —

We discuss in this Appendix the uncertainties of the effective number approach used to calculate the cross sections. As we can see from the data in Ref. 7) and the theoretical prediction in Ref. 12), the effective number approach works well to predict the shape of the  $(d, {}^3\text{He})$  spectra, however, it fails to predict the absolute magnitude of the cross sections correctly. Thus, it is important to know the limitation of the applicability of this approach. This is also important to apply this approach to deduce  $Z_\pi^*$  from experimental data as discussed in Section 3.3.

We show first the dependence of the calculated cross sections on the neutron wave functions  $\psi_n$  in targets. As mentioned in Appendix A, we adopted the HO wave functions for simplicity in this article. We calculate here the formation spectra using another set of  $\psi_n$  obtained by a theoretical potential Set OB in Ref. 41). The both neutron wave functions in  $3s_{1/2}$  state in  ${}^{120}\text{Sn}$  are shown in Fig. 9 as an example. The  ${}^{120}\text{Sn}$  target nucleus was used in the latest experiment<sup>7)</sup> and considered in the theoretical calculations<sup>11), 12)</sup> before. The  $3s_{1/2}$  neutrons have dominant contributions to the cross section coupled with pionic  $s$ -states. We can see in Fig. 9 that the both wave functions show similar behavior, however the wave function calculated by the potential in Ref. 41) has a little longer tail than that of the HO. Because of the distortion effects, the long range tail part of the wave function can be important for evaluating the formation rate.

Using these wave functions, we have calculated the  ${}^{120}\text{Sn}$   $(d, {}^3\text{He})$  spectra for the pionic atom formation and showed the results in Fig. 10. The  $F_O$  and  $F_R$  factors appeared in Eq. (A.13) are taken from Table IV in Ref. 12). We found that the cross sections calculated with  $\psi_n$  of Ref. 41) is about factor 3 larger than those with the harmonic oscillator. The theoretical calculations in Refs. 11), 12), which adopted the same harmonic oscillator wave functions for  $\psi_n$  with different parameterization of proton and neutron density distributions in  $V_{\text{opt}}$ , show the similar values for cross sections with the present case of HO wave functions, while the experimental result in Ref. 7) shows the smaller strength than theoretical calculations. We think that the tail part of the wave function is significantly important to evaluate the formation cross sections because the inner part of the wave function is masked by the distortion effects. And at the same time, it will be very difficult to obtain the tail of  $\psi_n$  precisely and to make the accurate predictions of the absolute values of the formation cross sections. On the other hand, the shape of the spectra is relatively robust and is insensitive to  $\psi_n$  as shown in Fig. 10. Thus, it is better to use the ratio of the formation rates of  $1s$  and  $2s$ , for example, to deduce the information of  $Z_\pi^*$  than to use the absolute peak height of each state to reduce the uncertainties due to  $\psi_n$ . The variation of the ratio of the effective numbers for the subcomponents  $[(1s)_\pi \otimes (3s_{1/2})_n^{-1}]$  and  $[(2s)_\pi \otimes (3s_{1/2})_n^{-1}]$  due to the different neutron wave functions is around 10 % for the case in Fig. 10.

We then consider the uncertainties due to the neutron occupation probability ( $F_O$ ) in the target nucleus and the relative strength of the excited levels ( $F_R$ ) of the

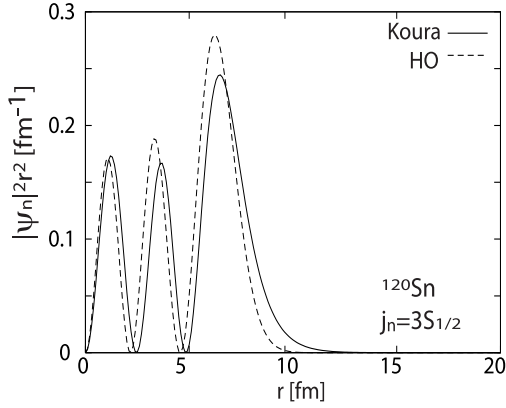


Fig. 9. Neutron distributions of  $j_n = 3s_{1/2}$  state in  $^{120}\text{Sn}$  by the harmonic oscillator wave function (dashed line) and the calculated wave function by the potential (set OB) in Ref 41) (solid line).

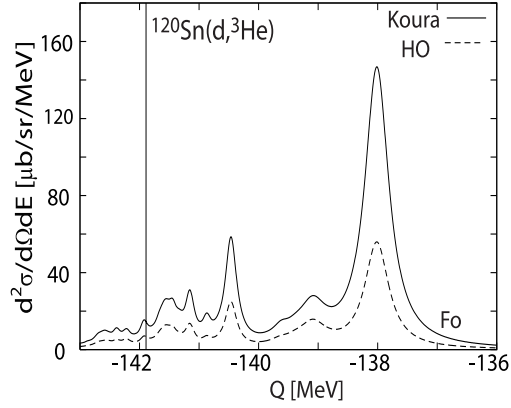


Fig. 10. Expected spectra of the  $^{120}\text{Sn}(d, ^3\text{He})$  reaction for the formation of deeply bound pionic atoms at  $T_d = 500$  MeV plotted as functions of the reaction  $Q$ -value. The harmonic oscillator (dashed line) and the theoretical (solid line) neutron wave functions<sup>41)</sup> are used. Instrumental energy resolution is assumed to be 150 keV FWHM. The vertical line indicates the threshold  $Q = -141.9$  MeV.

daughter nucleus. We summarize  $F_O$  and  $F_R$  together with the excited energies ( $E_x$ ) in Table V and VI.  $F_R$  and  $E_x$  of  $^{119,123}\text{Sn}$  can be found in Table IV of Ref. 12). We show three sets of  $F_O$  values in Table V to estimate the uncertainties of the  $F_O$  values. Within these neutron states, it is known that the  $s_{1/2}$  and  $d_{5/2}$  states have dominant contributions to the  $(d, ^3\text{He})$  spectra in recoilless kinematics for the pionic atom formation. As we can see from Table V, the calculated results by RMF model with and without including the possibility of nuclear deformation ( $F_O^d$  and  $F_O^s$ ) show the qualitatively same results. This fact indicates that these Sn isotopes are almost spherical nuclei. In addition,  $F_O$  obtained from experimental data also show similar results. On the other hand, the results of Te isotopes show significantly different and complicated features as shown in Appendix D. Thus, the uncertainties due to  $F_O$  for Sn isotopes, which are roughly 20-30 %, are much smaller than those for Te isotopes. This ambiguity, however, does not affect the ratio between subcomponents with the same neutron hole state.

As for the excited states of the daughter nuclei of the  $(d, ^3\text{He})$  reaction, the relative strength  $F_R$  is listed in Table VI for  $^{121}\text{Sn}$  and in Table IV of Ref. 12) for  $^{119,123}\text{Sn}$ . It is difficult to evaluate the systematic errors of these numbers. We can say, however, that the strengths of the excited states of Sn isotopes are suited for the pionic atom formation because of their simplicity. The only  $2d_{5/2}$  excited level of  $^{119,121,123}\text{Sn}$  isotopes has a little complex structure including a few levels, however, there is a clear dominant level with the largest value of  $F_R$  even for the  $d_{5/2}$ . On the other hand the excited levels in  $^{121,125}\text{Te}$  include several levels of the

Table V. Normalization factors, which correspond to the occupation probability of each neutron state for the ground state of the target nucleus, are shown for  $^{120}\text{Sn}$ ,  $^{122}\text{Sn}$ , and  $^{124}\text{Sn}$  nuclei. The normalization factors indicated by  $F_O$  are evaluated by experimental data.<sup>12), 42)</sup>  $F_O^s$  and  $F_O^d$  are obtained by the theoretical calculations of RMF model.<sup>43)</sup>  $F_O^s$  is calculated by assuming the spherical shape of nuclei, and  $F_O^d$  by including the deformation effects. The numbers with asterisk for  $1g_{7/2}$  and  $1h_{11/2}$  states are estimated so as to satisfy the normalization of total neutron number in the valence shells by assuming the same occupation probabilities for both states.

$F_O$	$^{120}\text{Sn}$	$^{122}\text{Sn}$	$^{124}\text{Sn}$	$F_O^s$	$^{120}\text{Sn}$	$^{122}\text{Sn}$	$^{124}\text{Sn}$	$F_O^d$	$^{120}\text{Sn}$	$^{122}\text{Sn}$	$^{124}\text{Sn}$
Neutron orbit				Neutron orbit				Neutron orbit			
$3s_{1/2}$	0.70	0.73	0.80	$3s_{1/2}$	0.54	0.65	0.78	$3s_{1/2}$	0.53	0.67	0.78
$2d_{3/2}$	0.50	0.51	0.69	$2d_{3/2}$	0.64	0.77	0.85	$2d_{3/2}$	0.68	0.76	0.85
$2d_{5/2}$	0.94	0.86	0.94	$2d_{5/2}$	0.93	0.95	0.96	$2d_{5/2}$	0.94	0.95	0.96
$1g_{7/2}$	0.70	0.67*	0.70*	$1g_{7/2}$	0.95	0.98	0.97	$1g_{7/2}$	0.97	0.97	0.97
$1h_{11/2}$	0.42	0.67*	0.70*	$1h_{11/2}$	0.28	0.33	0.47	$1h_{11/2}$	0.24	0.35	0.45

same quantum numbers with comparable strength as shown in Appendix D, which makes the reaction spectra rather complicated and prevents us from deducing the information on pion. Thus, we can say that the Sn isotopes are more suited as the targets of the  $(d, {}^3\text{He})$  reactions for the formations of the pionic atoms.

Table VI. Excitation energy ( $E_x$ ) and relative strength ( $F_R$ ) of each excited level in  $^{121}\text{Sn}$  determined from the experimental data of Ref. 42).

$^{121}\text{Sn}$		
Neutron hole orbit	$E_x$ [MeV]	$F_R$
$3s_{1/2}$	0.06	1.00
$2d_{3/2}$	0.00	1.00
$2d_{5/2}$	1.11	0.65
	1.37	0.35
$1g_{7/2}$	0.90	1.00
$1h_{11/2}$	0.05	1.00

### Appendix C

#### —— Structure of Pionic Atoms in $^{121}\text{Sn}$ and the Effective Nuclear Density probed by Atomic Pion ——

We show the calculated binding energies and widths in Table VII for  $\pi^-$  atoms in  $^{121}\text{Sn}$  nucleus, which are expected to be observed in near future at RIKEN/RIBF.<sup>14), 15)</sup> We find, as the previous works<sup>2), 3), 11), 12)</sup> showed, that the optical potential acts as the soft repulsive core and moved pionic wave functions outwards. This effect makes the widths of the bound states smaller to be quasi-stable states. As we can see from Table VII, the eigen energies of pionic bound states are spread in wide region such as  $250 \lesssim \text{B.E.} \lesssim 3800$  [keV] and  $10^{-3} \lesssim \Gamma \lesssim 320$  [keV] for the

Table VII. Calculated binding energies B.E. and widths  $\Gamma$  of  $\pi^- - {}^{121}\text{Sn}$  atom in units of keV. B.E.<sub>FC</sub> indicates the binding energies calculated with a finite-size Coulomb potential only.

state	$\pi^- - {}^{121}\text{Sn}$		
	B.E. <sub>FC</sub> [keV]	B.E. [keV]	$\Gamma$ [keV]
1s	6227.7	3829.2	320.6
2s	1913.9	1415.6	76.8
3s	909.2	732.5	29.3
4s	528.3	446.6	14.1
5s	344.7	300.5	7.8
6s	242.4	215.8	4.8
2p	2321.2	2262.7	116.7
3p	1034.9	1013.6	39.6
4p	582.5	572.9	17.5
5p	372.8	367.7	9.2
6p	258.8	255.8	5.4
3d	1037.8	1040.5	2.5
4d	584.0	585.6	1.5
5d	373.6	374.6	$9.0 \times 10^{-1}$
6d	259.3	259.9	$5.6 \times 10^{-1}$
4f	581.8	581.8	$5.6 \times 10^{-3}$
5f	372.5	372.5	$4.8 \times 10^{-3}$
6f	258.7	258.7	$3.5 \times 10^{-3}$

states with principal quantum number  $n = 1 \sim 6$ , and the shapes of pion densities are changed significantly for different states.

We, then, consider the effective nuclear density probed by atomic pion, which was proposed in Ref. 28) and was one of the good quantities to know the nuclear density sensitively observed by pion in atomic states. The definition of the effective nuclear density  $\rho_e$  and the overlapping density  $S(r)$  are given in Section 3.2 and Ref. 28). We show as an example calculated pion densities  $|R|^2$ , nuclear density  $\rho$ , and the overlapping densities  $S$  for 1s and 2s states in  ${}^{121}\text{Sn}-\pi^-$  atoms in Fig. 11. We find the same tendency as found in Ref. 28) for different systems. Namely, the peak positions of the overlapping density  $S(r)$  and, thus, the effective density  $\rho_e$  values are almost same for 1s and 2s atomic states even their eigen energies and wave functions are much different. We can interpret this tendency by considering the fact that the repulsive optical potential and the attractive Coulomb potential make the potential pocket at nuclear surface, where the overlapping densities are localized.

## Appendix D

### — Numerical results for Te isotopes —

We show in this Appendix that the calculated results for Te isotopes, which are candidate nuclei of the future pionic atom experiments in RIBF/RIKEN.<sup>14), 15)</sup> In Table VIII, we show the calculated results of the binding energies and widths of the pionic states in  ${}^{121}\text{Te}$  and  ${}^{125}\text{Te}$ . We find that the level spacing is larger enough than the level widths and the states are quasi-stable as other deeply bound pionic atoms.

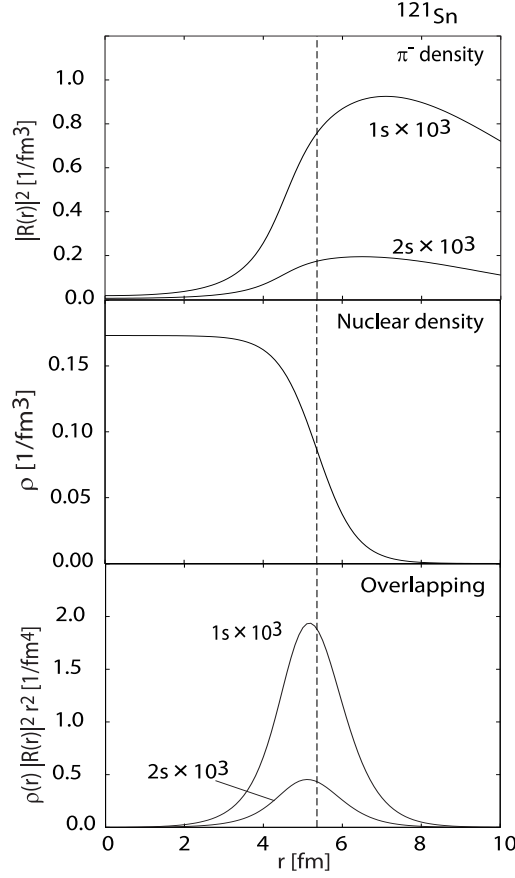


Fig. 11. Overlapping densities (lower frame) of the  $\pi^-$  densities (upper frame) with the nuclear density (middle frame) in pionic bound  $1s$  and  $2s$  states in  $^{121}\text{Sn}$ . The vertical broken line shows the half-density radius of the nuclear density of  $^{121}\text{Sn}$ .

In Table IX, we show the occupation probabilities ( $F_O$ ) of the target nuclei  $^{122}\text{Te}$  and  $^{126}\text{Te}$ . The factor  $F_O$  evaluated with the experiment is listed together with theoretical values,  $F_O^s$  and  $F_O^d$ . As you can see in the tables, the occupation of  $3s_{1/2}$  is significantly depend on the evaluation method. Since  $F_O^d$  is much smaller than  $F_O^s$  for the  $3s_{1/2}$  level, we can expect that both  $^{122}\text{Te}$  and  $^{126}\text{Te}$  are largely deformed. However, the experimental  $F_O$  based on Ref. 44) are closer to the spherical nuclear value  $F_O^s$ . This feature seems somehow inconsistent, and these numbers could include large errors. Actually larger deformations for Te isotopes than Sn isotopes were reported in Ref. 45). In Table X, we show the relative strength  $F_R$  for excited levels of daughter nuclei  $^{121}\text{Te}$  and  $^{125}\text{Te}$ . Here, we can see that the level structures of both nuclei are a little complicated. Especially, the  $2d_{5/2}$  state splits into several levels, which include plural levels with similar strength. These structures may cause extra difficulties to deduce the pion properties from the formation spectra of the pionic atoms.

We show in Fig. 12 the calculated  $(d, {}^3\text{He})$  spectra for the  $^{122}\text{Te}$  and  $^{126}\text{Te}$  targets.



Table VIII. Calculated binding energies B.E. and widths  $\Gamma$  of  $\pi^- - {}^{121}\text{Te}$  and  $\pi^- - {}^{125}\text{Te}$  atoms in units of keV.

state	$\pi^- - {}^{121}\text{Te}$		$\pi^- - {}^{125}\text{Te}$	
	B.E. [keV]	$\Gamma$ [keV]	B.E. [keV]	$\Gamma$ [keV]
1s	4096.3	372.5	4037.1	342.4
2s	1522.0	93.3	1507.3	84.1
3s	789.1	36.2	783.4	32.5
4s	481.6	17.6	478.9	15.7
5s	324.2	9.8	322.7	8.8
6s	233.0	6.0	232.1	5.4
2p	2445.2	141.9	2432.7	133.7
3p	1095.8	48.4	1091.4	45.4
4p	619.4	21.5	617.5	20.1
5p	397.6	11.3	396.6	10.5
6p	276.7	6.6	276.1	6.2
3d	1126.6	3.3	1126.7	3.4
4d	634.1	2.0	634.1	2.1
5d	405.5	1.2	405.6	1.2
6d	281.4	$7.5 \times 10^{-1}$	281.4	$7.6 \times 10^{-1}$
4f	629.5	$8.0 \times 10^{-3}$	629.5	$8.5 \times 10^{-3}$
5f	403.0	$6.9 \times 10^{-3}$	403.1	$7.3 \times 10^{-3}$
6f	279.9	$5.1 \times 10^{-3}$	279.9	$5.4 \times 10^{-3}$

Table IX. Normalization factors, which correspond to the occupation probability of each neutron state for the ground state of the nucleus, are shown for  ${}^{122}\text{Te}$  and  ${}^{126}\text{Te}$  nuclei. The normalization factors indicated by  $F_O$  are evaluated by experimental data.<sup>44)</sup> The normalization factors  $F_O^s$  and  $F_O^d$  are obtained by the theoretical calculations of RMF model.<sup>43)</sup> The factor  $F_O^s$  is calculated by assuming the spherical shape of nuclei, and  $F_O^d$  by including the deformation effects.

$F_O$			$F_O^s$			$F_O^d$		
Neutron	${}^{122}\text{Te}$	${}^{126}\text{Te}$	Neutron	${}^{122}\text{Te}$	${}^{126}\text{Te}$	Neutron	${}^{122}\text{Te}$	${}^{126}\text{Te}$
orbit			orbit			orbit		
$3s_{1/2}$	0.34	0.50	$3s_{1/2}$	0.41	0.69	$3s_{1/2}$	0.02	0.05
$2d_{3/2}$	0.31	0.47	$2d_{3/2}$	0.58	0.80	$2d_{3/2}$	0.36	0.85
$2d_{5/2}$	0.65	1.00	$2d_{5/2}$	0.90	0.95	$2d_{5/2}$	0.95	0.98
$1g_{7/2}$	0.43	0.59	$1g_{7/2}$	0.96	0.97	$1g_{7/2}$	0.98	0.99
$1h_{11/2}$	0.23	0.42	$1h_{11/2}$	0.33	0.51	$1h_{11/2}$	0.41	0.56

We find that the shape of the calculated spectra strongly depends on the choice of  $F_O$  as we expected. The results with  $F_O$  and  $F_O^s$  show the qualitatively same behavior, however, the results with  $F_O^d$  show the much different behavior. This is due to the smallness of  $F_O^d$  for  $3s_{1/2}$  neutron state, which can have dominant contribution to the spectra coupled with the pionic  $s$ -states in the recoilless kinematics. The lack of the  $3s_{1/2}$  neutron contribution deformed the shape of the spectra drastically. In the spectra calculated with  $F_O^d$ , the contributions of many subcomponents compose the total spectra and, hence, they make it difficult to deduce pion information clearly

Table X. Excitation energy ( $E_x$ ) and relative strength ( $F_R$ ) of each excited level in  $^{121}\text{Te}$  and  $^{125}\text{Te}$  determined from the experimental data of Ref. 44).

$^{121}\text{Te}$			$^{125}\text{Te}$		
Neutron hole orbit	$E_x[\text{MeV}]$	$F_R$	Neutron hole orbit	$E_x[\text{MeV}]$	$F_R$
$3s_{1/2}$	0.00	1.00	$3s_{1/2}$	0.00	1.00
$2d_{3/2}$	0.21	1.00	$2d_{3/2}$	0.04	1.00
$2d_{5/2}$	0.48	0.37	$2d_{5/2}$	0.64	0.35
	0.59	0.28		1.05	0.19
	0.92	0.09		1.14	0.19
	1.17	0.15		1.27	0.15
	1.32	0.05		1.43	0.11
	1.36	0.06	$1g_{7/2}$	0.64	0.73
$1g_{7/2}$	0.45	0.71		1.74	0.27
	1.15	0.29	$1h_{11/2}$	0.00	1.00
$1h_{11/2}$	0.29	1.00			

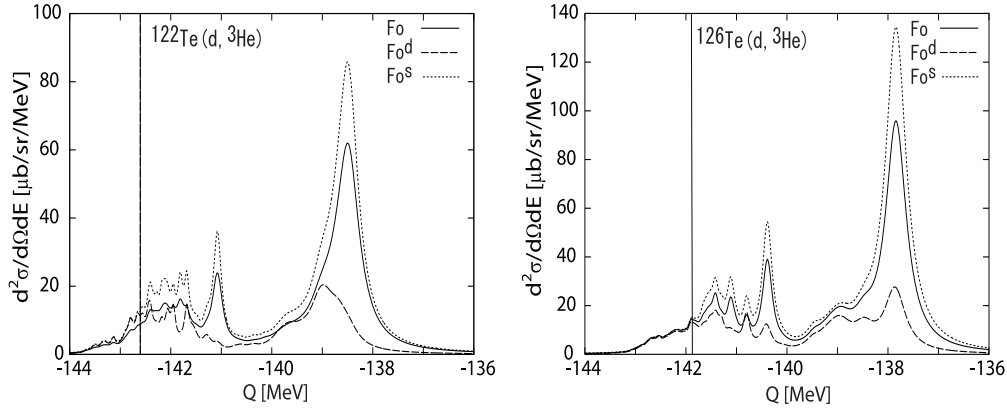


Fig. 12. Calculated  $^{122}\text{Te}(d,^3\text{He})$  (left) and  $^{126}\text{Te}(d,^3\text{He})$  (right) spectra for the formation of the pionic bound states at  $T_d = 500\text{MeV}$  are shown as functions of the reaction  $Q$ -value. Each line indicates the result with the different normalization factors ( $F_O, F_O^d, F_O^s$ ) shown in Table IX. The vertical line indicated the threshold  $Q = -142.6\text{ MeV}$  (left) and  $-141.9\text{ MeV}$  (right).

from the total spectra in this case.

Thus, we can conclude here that the expected spectra of the  $(d,^3\text{He})$  reaction on the Te isotope targets for the pionic atom formation mentioned in Ref. 14) could include large uncertainties due to nuclear structure which should be considered carefully before experiments.

### References

- 1) T. Hatsuda and T. Kunihiro, Phys. Rept. **247** (1994), 221, and references therein.
- 2) H. Toki and T. Yamazaki, Phys. Lett. **B213** (1988), 129.
- 3) H. Toki, S. Hirenzaki, T. Yamazaki and R.S. Hayano Nucl. Phys. **A501** (1989), 653.
- 4) H. Gilg *et al.*, Phys. Rev. **C62** (2000), 025201.
- 5) K. Itahashi *et al.*, Phys. Rev. **C62** (2000), 025202.
- 6) H. Geissel *et al.*, Phys. Lett. **B549** (2002), 64.

- 7) K. Suzuki *et al.*, Phys. Rev. Lett. **92** (2004), 072302.
- 8) S. Hirenzaki, H. Toki and T. Yamazaki, Phys. Rev. **C44** (1991), 2472.
- 9) H. Toki, S. Hirenzaki and T. Yamazaki, Nucle. Phys. **A530** (1991), 679.
- 10) S. Hirenzaki and H. Toki, Phys. Rev. **C55** (1997), 2719.
- 11) Y. Umemoto, S. Hirenzaki and K. Kume, Prog. Theor. Phys. **103** (2000), 337.
- 12) Y. Umemoto, S. Hirenzaki, K. Kume and H. Toki, Phys. Rev. **C62** (2000), 024606.
- 13) D. Jido, T. Hatsuda and T. Kunihiro, Phys. Lett. **B670** (2008), 109.
- 14) K. Itahashi *et al.*, 'Precision Spectroscopy of Pionic Atoms in ( $d, {}^3\text{He}$ ) Nuclear Reactions'; Exp. proposal NP0702-RIBF-027 for RIBF, Dec. (2006).
- 15) K. Itahashi *et al.*, 'Spectroscopy of Pionic Atom in  ${}^{122}\text{Sn}(d, {}^3\text{He})$  Nuclear Reaction'; Exp. proposal NP0802-RIBF-054 for RIBF, Jan. (2008).
- 16) T. Yamazaki *et al.*, Z. Phys. **A355** (1996), 219.
- 17) H. Toki, S. Hirenzaki, and K. Takahashi, Z. Phys. **A356** (1997), 359.
- 18) E. E. Kolomeitsev, N. Kaiser and W. Weise, Phys. Rev. Lett. **90** (2003), 092501.
- 19) T. Hatsuda and T. Kunihiro, Prog. Theor. Phys. **74** (1985), 765.
- 20) U. Vogl and W. Weise, Prog. Part. Nucl. Phys. **27** (1991), 195.
- 21) M. Gell-Mann, R. J. Oakes and B. Renner, Phys. Rev. **C175** (1968), 2195.
- 22) Y. Tomozawa, Nuovo Cim. **46A** (1966), 707.
- 23) S. Weinberg, Phys. Rev. Lett. **17** (1966), 616.
- 24) D. Jido, T. Hatsuda and T. Kunihiro, Phys. Rev. **D63** (2001), 011901.
- 25) U. G. Meissner, J. A. Oller, A. Wirzba, Ann. Phys. **297** (2002), 27.
- 26) M. Doring, E. Oset, Phys. Rev. **C77** (2008), 024602.
- 27) N. Kaiser, P. de Homont, W. Weise, Phys. Rev. **C77** (2008), 025204.
- 28) T. Yamazaki and S. Hirenzaki, Phys. Lett. **B557** (2003), 20.
- 29) R. Seki, K. Masutani, Phys. Rev. **C27** (1983), 2799.
- 30) T. Kubo, Nucl. Instr. Meth. in Phys. Res. B **204** (2003), 97.
- 31) S. Itoh *et al.*, RIKEN Accel. Prog. Rep. **43** (2010), 191.
- 32) C. J. Batty, E. Friedman and A. Gal, Phys. Rep. **287** (1997), 385;  
E. Friedman and A. Gal, Phys. Rep. **452** (2007), 89.
- 33) E. Friedman and G. Soff, J. of Phys. **G11** (1985), L37.
- 34) H. Toki, S. Hirenzaki and T. Yamazaki, Phys. Lett. **B249** (1990), 391.
- 35) S. Hirenzaki, T. Kajino, K. I. Kubo, H. Toki and I. Tanihata, Phys. Lett. **B194** (1987), 20.
- 36) M. Fujita, S. Hirenzaki and K. Kume, Phys. Rev. **C67** (2003), 034605.
- 37) Y. Umemoto, S. Hirenzaki, K. Kume, H. Toki and I. Tanihata, Nucl. Phys. **A679** (2001), 549.
- 38) G. Fricke and C. Bernhardt, ATOMIC DATA AND NUCLEAR DATA TABLES 60 (1995), 177.
- 39) M. Ericson and T. E. O. Ericson, Ann. Phys. (NY), **36** (1966) 496.
- 40) J. Nieves, E. Oset and C. Garcia-Recio, Nucl. Phys. **A554** (1993), 509.
- 41) H. Koura, M. Yamada, Nucl. Phys. **A671** (2000), 96.
- 42) E. J. Schneid, A. Prakash, and B. L. Cohen, Phys. Rev. **156** (1967), 1316.
- 43) L. Geng, H. Toki, S. Sugimoto, and J. Meng, Prog. Theor. Phys. **110** (2003), 921.
- 44) M. A. G. Fernandes and M. N. Rao, J. Phys. G: Nucl. Phys. **3** (1977), 1397.
- 45) S. Raman, C. W. Nestor, Jr., and P. Tikkanen, Atomic Data and Nuclear Data Tables **78** (2001), 1.